3D variable-density SPARKLING trajectories for high-resolution T2*-weighted Magnetic Resonance imaging

Carole Lazarus, Pierre Weiss, Loubna El Gueddari,
Franck Mauconduit, Alexandre Vignaud and Philippe Ciuciu

***Abstract*—We have recently proposed a new optimization algorithm called SPARKLING (Spreading Projection Algorithm for Rapid K-space sampLING) to design efficient Compressive Sampling patterns for Magnetic Resonance Imaging. This method has a few advantages over conventional non-Cartesian trajectories such as radial lines or spirals: i) it allows to sample the k-space along any arbitrary density while the other two are restricted to radial densities and ii) it achieves a higher image quality for a given readout time. Here, we introduce an extension of the SPARKLING method for 3D imaging by considering both stacks-of-SPARKLING and fully 3D SPARKLING trajectories. Our method allowed to achieve an isotropic resolution of 600 μm in just 45 seconds, compared to a scan duration of 14 min 31 s using 4-fold accelerated parallel imaging, for T2*-weighted *ex vivo* brain imaging at 7 Tesla over a field-of-view of $200 \times 200 \times 140$ mm^3.**

***Index Terms*—3D MRI, optimization, non-Cartesian, compressed sensing, acceleration, SWI.**

I. Introduction

To reduce scan time in MRI, sampling along non-Cartesian trajectories may prove to be advantageous. An efficient use of the MR gradient hardware can indeed enable rapid coverage of the k-space. When combined with compressed sensing, the use of undersampled non-Cartesian trajectories can allow further reduction in the acquisition time [1]. In this context, it was shown that k-space trajectories should perform a variable density sampling for best performance [2]–[4].

Three-dimensional (3D) compressed acquisitions are usually performed with 3D radial trajectories [5] or Poisson Disk lines [6]. The former observes a fully 3D variable density while the latter performs a 2D Poisson disk variable density orthogonally to the readout lines. Let us mention a few other fully 3D sampling strategies based on analytical expression such as 3D cones [7], twisted projections (TPI) [8], Stacks of Spirals [9] and hybrid radial-cones [10]. These methods are restricted to different types of sampling densities (e.g. radial or cylindrical), which is a critical element for efficiency. A few works attempted to use optimization principles to design 3D trajectories [11]–[13], but did not include clear sampling criteria.

Recently, we introduced a new optimization-driven method named SPARKLING (Spreading Projection Algorithm for Rapid K-space samplING) [14]–[16]. This algorithm inspired from stippling techniques automatically generates optimized non-Cartesian sampling patterns compatible with MR hardware constraints on maximum gradient amplitude and slew rate. These sampling curves are designed to comply with key criteria for optimal sampling: a controlled distribution of samples (e.g., a variable density) and a locally uniform k-space coverage. The SPARKLING strategy was used for 2D T_2^* high-resolution *in vivo* brain imaging and was shown to yield higher image quality compared to conventional non-Cartesian geometrical patterns such as radial or spiral trajectories, while allowing to reduce scan time by a factor up to 20 compared to standard Cartesian scans [16]. The proposed method may hence improve the trade-off between sampling efficiency and robustness to artifacts.

In this paper, we explore how the principles of the SPARKLING method can be extended to design 3D trajectories, expecting to benefit from higher signal-to-noise ratio (SNR) conditions. We begin by exploring the use of stack of 2D trajectories (such as stack of stars [17], [18], stack of spirals [7], [19] or stack of EPI [20]). Then, we turn to fully 3D SPARKLING trajectories, which have the potential to respect a truly 3D variable density necessary for an optimal use of compressed sensing in 3D [21], [22].

We performed 3D prospective high-resolution *ex vivo* T_2^*-weighted MR acquisitions at 7 Tesla. Since the SPARKLING algorithm is able to significantly improve the initial input trajectory in the longer-readout regime, we worked with a readout duration of 15 ms, which is used in many T_2^*- or susceptibility-weighted protocols at 7 Tesla [23]–[25]. We compared our method against several standard 3D sampling strategies. We used Cartesian scans for ground truth images and we restricted our comparisons to two non-Cartesian trajectories which allow to perform variable density sampling in the context of compressed sensing: 3D radial [5] and Poisson Disk lines [6].

II. Optimization-driven design of sampling patterns in MRI

A. 2D k-space trajectories

A k-space trajectory is usually composed of several segments $\mathbf{k}(t) = (k_x(t), k_y(t))$, also referred to as shots, which are controlled by magnetic field gradients $\mathbf{G}(t) = (G_x(t), G_y(t))$ as follows:

$$\mathbf{k}(t) = \frac{\gamma}{2\pi} \int_0^t \mathbf{G}(\tau) d\tau \,, \tag{1}$$

where γ denotes the gyro-magnetic ratio. Hardware constraints on the maximum gradient amplitude (G_{max}) and slew rate (S_{max}) induce limitations in trajectory speed and acceleration. These limits can be expressed as inequality range constraints on each of the time points of the discrete waveform $\mathbf{k} = (\mathbf{k}[i])_{1 \leq i \leq p}$ where $\mathbf{k}[i] = (k_x[i], k_y[i]), \forall 1 \leq i \leq p$ and p is the number of gradient time-steps. Typically, rotation invariant speed and acceleration constraints can be expressed as follows:[1]

$$\|\dot{\mathbf{k}}\|_{2,\infty} < \frac{\gamma}{2\pi} G_{max} \quad \text{(2a)} \qquad \|\ddot{\mathbf{k}}\|_{2,\infty} < \frac{\gamma}{2\pi} S_{max} \quad \text{(2b)}$$

where $\|\mathbf{c}\|_{2,\infty} = \sup_{1 \leq i \leq p} \left(|\mathbf{c}_x[i]|^2 + |\mathbf{c}_y[i]|^2 \right)^{1/2}$ and

$$\begin{cases} \dot{\mathbf{k}}[i] &= \frac{\mathbf{k}[i] - \mathbf{k}[i-1]}{dt}, \\ \ddot{\mathbf{k}}[i] &= \frac{\mathbf{k}[i+1] - 2\mathbf{k}[i] + \mathbf{k}[i-1]}{dt^2} \end{cases} \tag{3}$$

Here dt is the gradient raster time and in practice it may be different from the dwell time Δt.

Following [16], we let $\mathcal{Q}_p$ denote the set of p-dimensional k-space discrete curves $\mathbf{k}$ respecting the aforementioned constraints (2). Note that $\mathcal{Q}_p$ can be completed to account for any affine constraint such as the specification of $\mathbf{k}$ at the echo-time (TE): $\mathbf{k}[TE] = 0$. In the context of multi-shot acquisitions, these constraints apply to every shot independently. In the next section, we briefly remind the minimization problem we solve in the SPARKLING algorithm framework [15], [16] to point out the challenges raised in 3D imaging afterwards.

B. The SPARKLING algorithm

Our objective is to minimize a ℓ_2 distance between a target density $\rho : \mathbb{R}^3 \to \mathbb{R}$ and a sampling trajectory $\mathbf{k}$ under the aforementioned constraints (2):

$$\min_{\mathbf{k} \in \mathcal{Q}_p} dist(\rho, \nu(\mathbf{k})) = \min_{\mathbf{k} \in \mathcal{Q}_p} \frac{1}{2} \|h \star (\nu(\mathbf{k}) - \rho)\|_2^2 \tag{4}$$

where h is a continuous interpolation kernel, symbol $\star$ denotes the convolution operator, $\nu(\mathbf{k})$ is the discrete measure supported by the curve $\mathbf{k}$ (see [14] for the definition of ν and more details). The distance in Eq. (4) can be conveniently rewritten by expanding the ℓ_2-norm into:

$$\min_{\mathbf{k} \in \mathcal{Q}_p} \underbrace{\frac{1}{p} \sum_{i=1}^{p} \int_\Omega H(x - \mathbf{k}[i]) \rho(x) \, dx}_{F_{\mathrm{a}}(\mathbf{k})} - \underbrace{\frac{1}{2p^2} \sum_{1 \leq i,j \leq p} H(\mathbf{k}[i] - \mathbf{k}[j])}_{F_{\mathrm{r}}(\mathbf{k})} \tag{5}$$

where Ω denotes the sampling domain, and the Fourier transform $\hat{H}$ of H is equal to $|\hat{h}|^2$. In our experiments, we selected the Euclidean distance $H(x) = \|x\|_2$ [15], [27]. Problem (5) can be interpreted as the minimization of a potential energy $F = F_{\mathrm{a}} - F_{\mathrm{r}}$ containing an attractive term F_{a} (bringing together samples according to the target density ρ) and a repulsive term F_r (avoiding the formation of gaps and clusters of samples). Although the cost function is non-convex, F_a and F_r are differentiable, so the calculation of their gradient (∇F_a and ∇F_r, respectively) is feasible, and the global cost function can be *locally* minimized by a projected gradient descent of the type $\mathbf{k}_{t+1} = \Pi_{\mathcal{Q}_p} (\mathbf{k}_t - \beta_t \nabla F(\mathbf{k}_t))$ where $\nabla F = \nabla F_a - \nabla F_r$. This algorithm alternates between a non-convex distance minimization part and a projection onto the convex MR constraints $\mathcal{Q}_p$. We refer to [28] for more details on the computation of the gradient ∇F and to [26] for details about the projection on $\mathcal{Q}_p$.

C. Stack-of-SPARKLING

A first strategy to perform 3D imaging with the SPARKLING method is to use 2D SPARKLING trajectories and stack them along the partition direction denoted here as z. This approach is illustrated in Fig. 1**a** for a stack of 10 identical SPARKLING trajectories, which will be referred to as *regular stack-of-SPARKLING* or *regular SoSPARKLING*. To respect the Nyquist criterion along the partition direction, the N_z SPARKLING planes should be spaced by a FOV_z^{-1}-distance until reaching the desired maximum spatial frequency. To increase the incorehence in the z-axis, these planes were rotated by the golden angle. In the situation of a regular SoSPARKLING, no variable density is performed along the partition direction.

More interestingly, to subsample the partition direction and obtain a fully 3D variable density, the target density may be changed according to the plane's altitude k_z. Given a 3D density $\rho \in \mathbb{R}^{N \times N \times N_z}$, a 2D SPARKLING trajectory at altitude k_z will be generated using the density $\rho_{2D}(k_z) = \frac{\rho(:,:,k_z)}{\int \rho(:,:,k_z)}$. In addition, once the number of shots in the central stack $n(0)$ is chosen, the mass of each plane can be adapted to the plane density by reducing the number of shots per altitude, as k_z increases:

$$n(k_z) = n(0) \frac{\int \rho(:,:,k_z)}{\int \rho(:,:,0)}, \tag{6}$$

where $n(k_z)$ is the number of shots in the plane of altitude k_z. Fig. 1**b** shows such a stack for an isotropic density (defined on a 3D ball) for 10 SPARKLING trajectories. This design will be referred to as *z-variable-density*

[1] In [26], we have also dealt with the case of rotation variant constraints where the ℓ_∞-norm replaces the mixed $\ell_{2,\infty}$-norm here.

stack-of-SPARKLING or *z-vd SoSPARKLING*. Further acceleration may be reached by subsampling the number of planes and using parallel imaging along this direction.

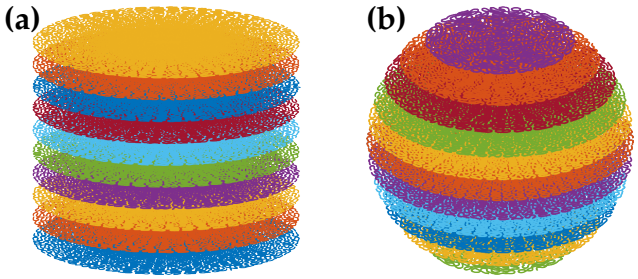

Fig. 1. Stack of 10 identical SPARKLING trajectories filling a cylinder (**a**) and stack of 11 variable SPARKLING trajectories filling a 3D ball (**b**). (Colors are just for visualization purposes).

D. Fully 3D SPARKLING

To perform a fully 3D sampling of the k-space, it is also possible to extend the SPARKLING algorithm presented in [15] to three dimensions. Such segmented sampling scheme is composed of non-Cartesian curves spanning all 3 k-space directions, filling a ball of radius k_{max}, where k_{max} is the maximum radial extent in the 3D k-space.

1) Algorithmic extension: The SPARKLING algorithm's bottleneck lies in the calculation of the gradient of the repulsive term F_r between the samples in Eq. (5), where there is a summation over all the samples. In 3D, this summation was calculated directly using a two-level nested loop, which gives a complexity of $O(p^2)$, where p is the number of particles in $\mathbf{k}$. For high resolution imaging, we need of the order of $p = 10^7$ particles, making this method irrelevant. The brute-force method could be accelerated using 3D techniques used for the simulation of particles (e.g. NFFT or fast multipole methods), but would require complex numerical libraries. In this work, since our objective is to target *radial densities*, which ensure rotation invariant reconstruction results, we propose an alternative technique described below.

2) Using a regular sphere tessellation to accelerate the process: The idea is to generate each shot independently from the others, by truncating the target density into n_s volumetric sectors filling the considered k-space, where n_s is the desired total number of shots. To further accelerate the process, we can reduce the number of SPARKLING-processed shots by using a semi-regular partition of the sphere. We used an equal-area tessellation which divides the sphere into regions of equal area [29], as is displayed in Fig. 2**a** for $n_s = 100$. The property of equal area is important insofar as it ensures that all 3D sectors have equal mass in the case of a radial density. Furthermore, for a constant elevation angle (highlighted in blue on Fig. 2**a**-**b**), all tiles are exactly identical and the associated trajectory can be obtained from another one using a simple rotation. Hence, only a small fraction of the desired total number of shots needs to be generated, namely one per latitude. This leads to a reduction in computation time by a factor 20 to 30. Using this strategy, the typical computational time to generate 1000 shots for a matrix size of $N = 256$ is about 20 minutes on a Intel Xeon(R) CPU at 2.20 GHz with 40 cores.

In the case of center-out shots, a 3D sector is created by connecting the four summits of a spherical tile to the origin of the k-space. If symmetric shots for which the echo time TE is at the middle of the segment, are desired, the latter sector constitutes one half of total symmetric sector and the other half is obtained by rotating the latter about the origin, as displayed in Fig. 2**b**. To avoid discontinuity between the two halves, the sector is slightly thickened near the origin. For example, with this strategy, only 7 symmetric shots need to be produced by the SPARKLING algorithm for $n_s = 100$. Fig. 2**b** shows one SPARKLING shot, corresponding to the highlighted sector for a radially decaying density and for a matrix size of $128 \times 128 \times 128$, $k_{max} = 320\,\mathrm{m}^{-1}$, $G_{max} = 40$ mT/m and $S_{max} = 200$ T/m/s. This shot is then rotated to fill the regions of equal elevation angle, as depicted in Fig. 2**c**. The process is repeated for all latitudes, generating the fully 3D SPARKLING trajectory shown in Fig. 2**d**.

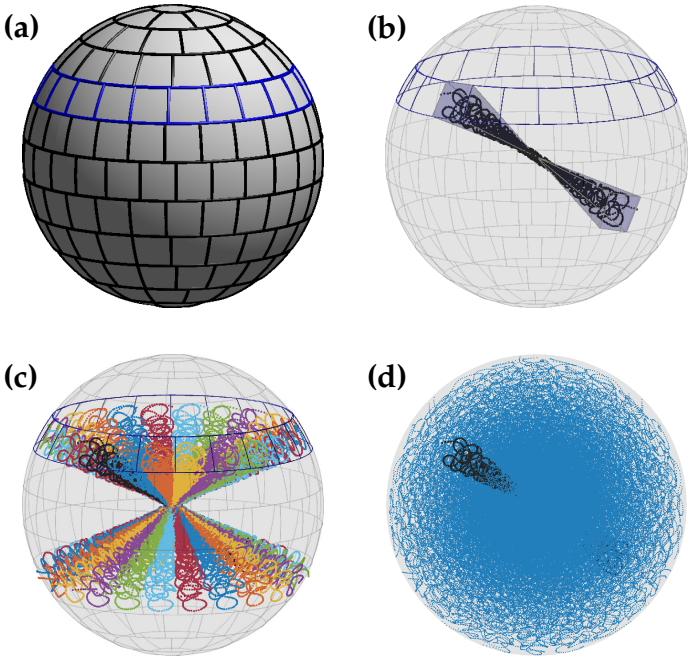

Fig. 2. 3D SPARKLING process. (**a**): Partition of the sphere into 100 regions of equal area. Regions along a constant elevation angle were highlighted in blue: they are identical up to a rotation. (**b**): One 3D density sector containing a SPARKLING shot. (**c**): The SPARKLING shot is then rotated along the considered latitude. (**d**): the whole fully 3D SPARKLING trajectory. An individual segment is highlighted in black. Parameters are: $N = 128$, $k_{max} = 320\,\mathrm{m}^{-1}$, 100 symmetric shots and 7 shots to generate (6 latitudes + 1 conic cap).

E. Selection of the target density

In view of the long computation time required for reconstructing 3D MR images (i.e. several hours), the

target density was retrospectively selected among a set of 6 radially decaying densities. We consider here a radial isotropic density of the form $\rho : \mathbf{k} \mapsto \frac{1}{|\mathbf{k}|^d}$, which decays as an inverse polynomial. Radial densities present the advantage of yielding results invariant to translation and rotation of the object to be imaged. The singularity at the origin is truncated by the method introduced in [16] allowing to create a circular plateau at Shannon's rate at the origin. Two parameters of the density were varied here: the decay rate $d \in \{2, 3\}$ and the plateau threshold $\tau \in \{0.5, 0.75, 1\}$. Fig. 3 shows the 6 tested densities for $N = 320$. To rank the different densities,

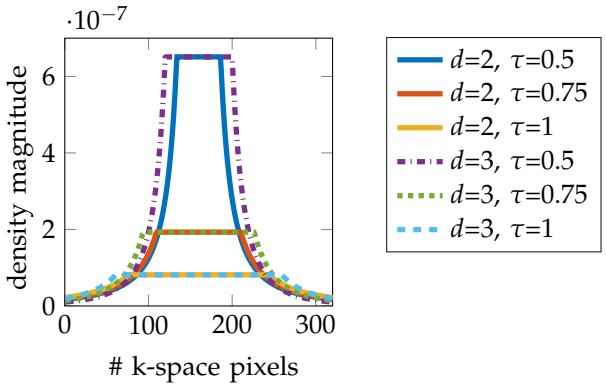

Fig. 3. 1D view of the 6 tested radial densities for $N = 320$. The x-axis is the pixel number while the y-axis is the amplitude of the density.

evenly spaced samples were drawn along each density by using Lloyd's algorithm, also known as Voronoi iteration [30]. Lloyd's method allows to quickly produce a distribution of points with blue noise characteristics, i.e. to produce a locally uniform coverage. The initial positions of the p samples were determined with an i.i.d. drawing along the considered density. Then, Lloyd's algorithm was applied using 10 cycles. Once the 3D samples are produced for $p = 10^6$ and all densities, the corresponding retrospectively generated Fourier data of a 3D baboon brain image are reconstructed using nonlinear 3D reconstructions (details about image reconstruction are provided in Section IV). The density which gives the best image quality both visually and in terms of pSNR is selected and will be used as a 3D target density for the SPARKLING trajectories. For instance, in the case of $N = 320$, we selected the density with $d = 3$ and $\tau = 0.75$.

III. Prospective 3D SPARKLING acquisition

3D acquisitions were performed on a 7 Tesla MR scanner (Siemens Healthineers, Erlangen, Germany) with a 1Tx/32Rx head coil (Nova Medical, Wilmington, MA, USA). The maximum gradient amplitude and slew rate for this system were 40 mT/m and 200 T/m/s, respectively. A 3D Gradient Recalled Echo (GRE) sequence was used. Following standard T2*-weighted and susceptibility-weighted protocols at 7 Tesla [23]–[25], we used an echo time TE=20 ms, a repetition time TR=40 ms

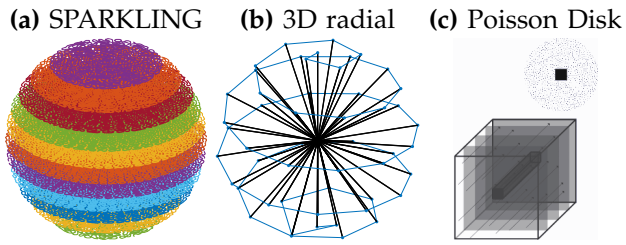

Fig. 4. The three 3D sampling schemes we compared: the proposed z-variable density SoSPARKLING **(a)**, the 3D radial-trajectories **(b)** [5] and the so-called Poisson Disk approach **(c)** proposed in [1], [6].

and a flip angle FA=15°. We took advantage of these parameters to acquire during a readout window of 15.36 ms with a receiver bandwith of 200 kHz. These parameters were kept constant for all different sampling schemes.

For different setups, prospective acquisitions were performed on an *ex vivo* baboon brain conserved in a fluorinert solution. All animal studies were conducted in accordance with the European convention for animal care and the NIHs Guide for the Care and Use of Laboratory Animals. First, for an isotropic resolution of 0.6 mm, the three proposed SPARKLING trajectories were compared: regular SoSPARKLING, z-vd SoSPARKLING and fully 3D SPARKLING. As reference, we also performed a standard Cartesian iPAT acquisition with GRAPPA reconstruction available on the scanner (Siemens product sequence) either for iPAT 4 (4x1 and 24 reference lines), iPAT 2 (24 references lines) with Partial Fourier 6/8 (phase and encode).

Furthermore, the 3D SPARKLING strategy was compared to other 3D trajectories used in compressed sensing MRI. First, the 3D Poisson disk strategy introduced by Lustig et al [6] was considered. This method, which will be referred to as *Poisson-disk-lines*, consists in acquiring along the partition direction cross-sections of 2D Poisson disk samples with a deterministic sampling of the k-space center (see Fig. 4**c**). We used the SPARKLING algorithm to generate this sampling, by disabling the constraints on speed and acceleration. The size of the deterministically sampled region and the radially decaying rate of the density outside this region were selected using a grid-search on retrospectively subsampled reconstructions of a brain phantom image, yielding a density with decay rate of $d = 3$ and a plateau threshold of $\tau = 1$. Second, 3D radial trajectories were also acquired for comparison [5] (see Fig. 4**b**). Since [16] already investigated the performance of 2D SPARKLING against radial and variable-density spiral trajectories, we did not investigate here the stack-of-stars nor the stack-of-spirals. We expect the relative performance of 2D sampling patterns to remain the same when they are stacked into 3D trajectories.

Finally, a high resolution of 0.3 mm in the axial plane with a slice thickness of 1.5 mm was performed, similar to the protocols presented in the literature [23], [25], [31]. Table I summarizes the studied protocols and the different acceleration setups. The acceleration factor AF

is calculated as a function of the fully-sampled Cartesian scan; it is given as the ratio of the number of lines in the reference scan over the number of shots in the accelerated scan (see its formula in Table I).

IV. 3D MR IMAGE RECONSTRUCTION

Images were reconstructed using a 3D extension of a self-calibrating reconstruction algorithm [32] that handles non-Cartesian k-space data collected over a multi-channel phased array and that promotes sparsity in the wavelet transform domain. The original code was implemented in Matlab and already used in [16] but an open source code is now available in Python in the PySAP software[2] both for 2D and 3D imaging. To speed up the reconstruction process in 3D imaging, the NFFT [33] was replaced with the GPU nufft[3]. Also, for the sake of efficiency, all 3D MR images were reconstructed using a Symmlet 8 orthogonal wavelet transform, an ℓ_1-sparsity promoting regularization. A FISTA algorithm was used to minimize the overall convex but nonsmooth objective function. For each dataset individually, the regularization parameter was grid searched over the range $(10^{-7}, 10^{-2})$ to optimize the structural similarity (SSIM) as a measure of image quality [35]. [4] Yet, the reconstruction time remained quite long, especially for treating 32 channel-receiver coil data, reaching about 4 hours for $N = 256$ and 400 iterations, including the calculation of the Lipschitz constant, with a NVIDIA GPU card GM204GL Quadro M4000 (1664 cores, global memory 8 GB).

V. RESULTS

A. Comparison of the different SPARKLING strategies

First, different 3D SPARKLING strategies were compared for an isotropic resolution of 0.6 mm. Regular SoSPARKLING, z-variable SoSPARKLING and fully 3D SPARKLING trajectories were acquired for two different acquisition times: 2 min 40 s and 1 min 22 s (see Table I for details on acquisition parameters). A Cartesian iPAT 4 scan (TA = 14 min 31 s) was also collected and will be considered as the reference image quality. Results in transversal, coronal, sagittal planes and a magnified central region of the axial slice are shown in Fig. 5 for a SPARKLING acquisition time of 2 min 40 s. Each column corresponds to a different sampling method.

For both scan times (see Supplementary Material Fig. 1 for 1 min 22 s results), the image quality is well preserved especially in the dendritic arborization in the cerebellum, which is visible in the sagittal plane. One may notice that the fully 3D SPARKLING results appear slightly blurrier than the SoSPARKLING results. Regular and z-variable SoSPARKLING yield similar image quality as is corroborated by the 3D SSIM scores measured with the iPAT 4 image as a reference.

B. Comparison with existing sampling trajectories

3D SPARKLING trajectories were also compared to 3D radial and Poisson disk sampling strategies for a very short acquisition time of 45 s, corresponding to a number of 1140 shots. Here, a z-variable-density stack-of-SPARKLING was used for SPARKLING acquisitions since it yielded better image quality among the previously tested 3D SPARKLING strategies and has the advantage of supporting high acceleration factor while still covering the low frequencies well. Indeed, at this acceleration factor, a regular SoSPARKLING would only have 5 shots per plane while the z-variable-density SoSPARKLING presents twice more shots in the center of the k-space. Moreover, a standard GRAPPA-accelerated Cartesian scans was also performed for an iPAT of 4 lasting 14 min 31 s. Results are shown in Fig. 6 for coronal, sagittal, axial planes and a magnified central region of the axial image. Each column corresponds to a different acquisition strategy.

Of all 45-second scans, the SPARKLING method presents the best image quality. For instance, the dendritic arborization in the cerebellum in the sagittal slice as well as the magnified region of the axial slice both appear significantly more blurry in 3D radial than in SPARKLING. Regarding the Poisson disk lines strategy, it is clearly not competitive in this setup as the high acceleration in time translates into a high in-plane subsampling factor in the phase encoding directions. These visual observations are corroborated by the SSIM scores: the SSIM of the SPARKLING image is increased by 20% compared to the 3D radial trajectories and by 50% for the Poisson disk trajectories.

C. High in plane resolution

Finally, images were acquired at a high in plane resolution of 0.3 mm with a slice thickness of 1.5 mm. A standard iPAT 2 PF 6/8 (phase and slice) scan was collected, which is commonly used in the literature of GRE for susceptibility weighted imaging (SWI) at 7 Tesla [23], and is shown in Fig. 7**a**. SPARKLING-accelerated acquisitions were also performed for an acquisition time of 2 min 43 s and 1 min 24 s as illustrated in Fig. 7**b**-**c**. Given the small number of slices in this application, we used a regular stack-of-SPARKLING for this acquisition. We can observe that the SPARKLING acquisitions yield good image quality although 4 and 10 times faster than the Cartesian scan, respectively.[5]

[2]https://github.com/CEA-COSMIC/pysap

[3]The Matlab API we used was developed by A. Schwarzl and F. Knoll, http://cai2r.net/resources/software/gpunufft-open-source-gpu-library-3d-gridding-direct-matlab-interface, whereas the one in Python was developed by J-M. Lin and is available in pynufft [34], cf https://github.com/jyhmiinlin/pynufft.

[4]The SSIM gives an image quality score relatively to a reference image. Its value lies between 0 and 1, the latter conveying a perfect match with the reference.

[5]The iPAT image in Fig. 7**a** which was reconstructed with the online scanner reconstructor presented a sub-pixel offset compared to the center of the image and the SPARKLING reconstructions, which is why SSIM scores were not calculated in this case.

TABLE I
ACQUISITION PARAMETERS USED FOR 3D K-SPACE TRAJECTORY DESIGN.

FOV (mm^3)	Matrix size	Resolution (mm)	Number of shots n_s	Total scan time (TA)	$AF = \frac{N \times N_z}{n_s}$
$200 \times 200 \times 140$	$320 \times 320 \times 224$	$0.6 \times 0.6 \times 0.6$	4010	2 min 40 s	18
			2050	1 min 22 s	35
			1140	45 s	63
$200 \times 200 \times 140$	$640 \times 640 \times 96$	$0.3 \times 0.3 \times 1.5$	4085	2 min 43 s	15
			2090	1 min 24 s	30

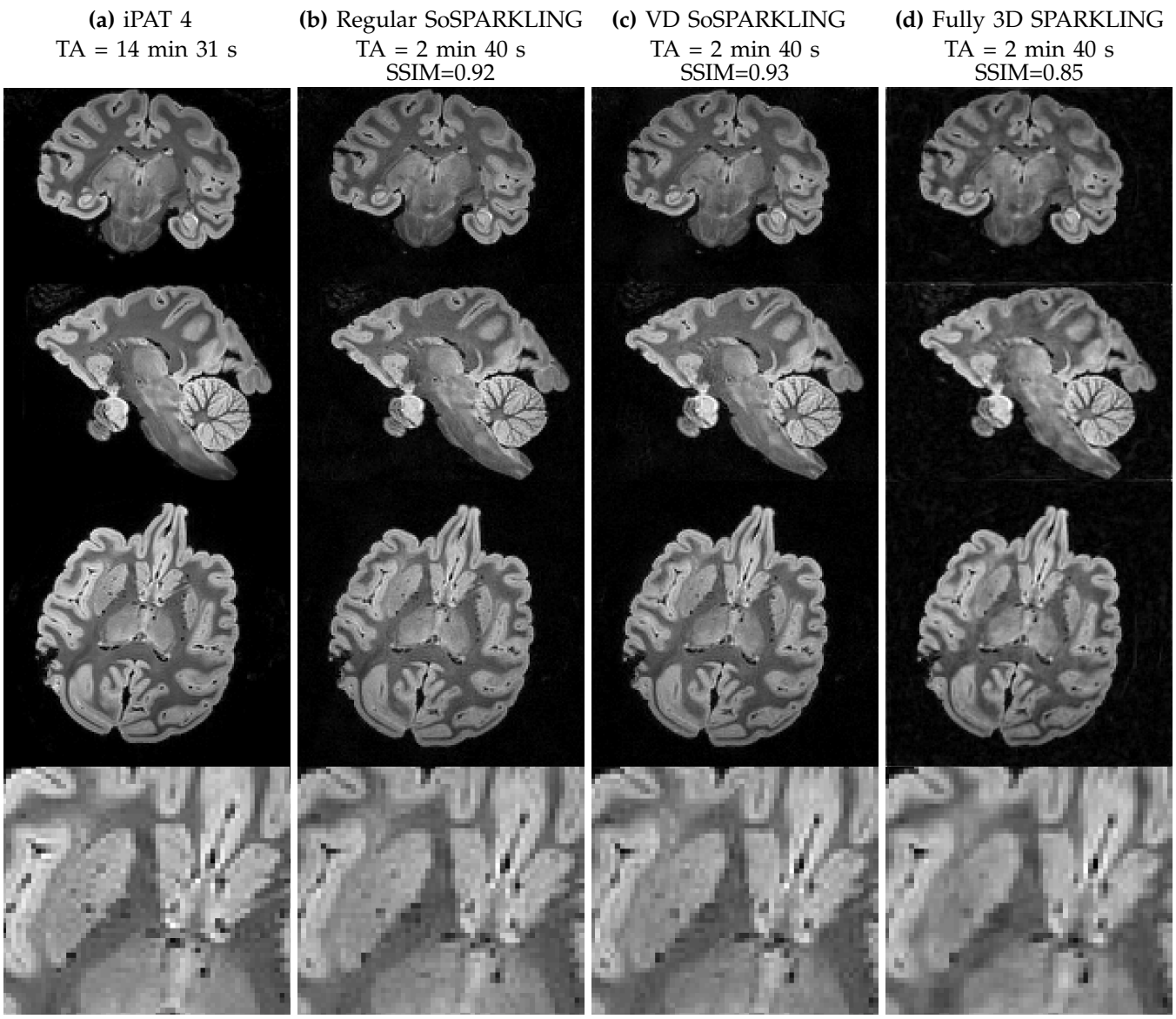

Fig. 5. **600 μm isotropic *ex vivo* results comparing different SPARKLING strategies**. Column (a): iPAT 4 (GRAPPA) acquisition lasting TA = 14 min 31 s. Column (b): regular stack-of-SPARKLING (SoSPARKLING) results for an acquisition time of TA = 2 min 40 s. Column (c): z-variable-density SoSPARKLING for an acquisition time of TA=2 min 40 s. Column (d): fully 3D SPARKLING for an acquisition time of TA = 2 min 40s. Rows 1 to 4 respectively display a coronal slice, a sagittal slice, an axial slice and a magnified region of the latter axial slice. FOV was $200 \times 200 \times 140$ mm^3.

VI. DISCUSSION

Among the three studied approaches of 3D SPARKLING (i.e., regular SoSPARKLING, z-variable-density SoSPARKLING and fully 3D SPARKLING), we observed that the z-variable-density SoSPARKLING was performing best. This strategy allows a variable density along the partition direction, thus allowing to trade high frequency contents for low frequency ones, in contrast to the regular SoSPARKLING. It thus pushes the undersampling factor even further.

Regarding the performance of the fully 3D

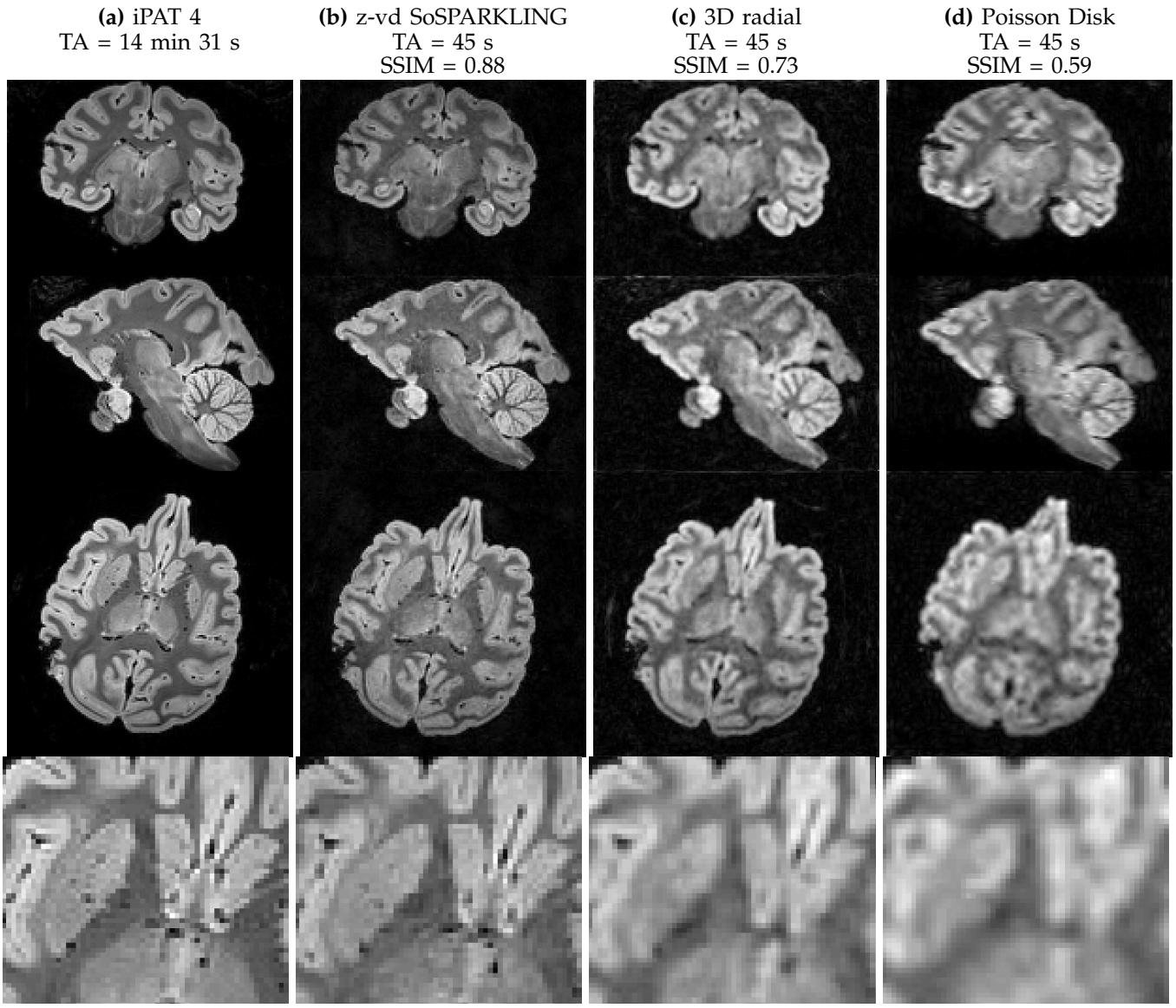

Fig. 6. *Ex vivo* results of 0.6 mm isotropic resolution comparing z-variable stack-of-sparkling (SoSPARKLING) **(b)**, 3D radial **(c)** and 3D Poisson-disk lines **(d)** samplings for a total number of shots of 1140, i.e., an acquisition time of 45 s. Reference scan in **(a)** is an iPAT 4 (GRAPPA) acquisition lasting TA = 14 min 31 s. FOV was $200 \times 200 \times 140$ mm^3.

SPARKLING which was slightly behind the SoSPARKLING strategies, one may propose several explanations. First, the constraint to generate the shots *separately* introduces some structure in the sampling, which leads to a degraded global distribution of the samples compared to 2D SPARKLING. To investigate this in more detail, it can be useful to look at all the samples of a 3D SPARKLING trajectory present in a plane of thickness one k-space pixel. These plane sections are shown in Fig. 8 for different axes and altitudes. Overall, asymmetric structures can be observed in these plane sections, due to the rotation of one SPARKLING-generated shot to fill one latitude of the k-space. In addition, the distribution of the samples is not as well controlled as it was for 2D SPARKLING, in terms of local uniformity for instance. Moreover, the center of the k-space seems to be critical as well: since the samples of different shots are not interacting, the global distribution of the samples in the center is not perfect, with possible under- or over-sampling. Hence, the fully 3D SPARKLING approach may be significantly improved by generating all the shots at once. This would however require a considerable development to maintain a reasonable computational time.

In this work, we used the accelerated 3D SPARKLING trajectories to acquire T_2^*-weighted images of an *ex vivo* baboon brain at a high isotropic resolution of 0.6 mm for a FOV of $200 \times 200 \times 140$ mm^3. If the iPAT 4 acquisition is considered as a reference scan, the proposed method allowed to divide the acquisition time by a factor of 20, reducing the scan time from 14 min 31 s to 45 s, while maintaining good image quality. For the studied imaging protocol, we also compared the SPARKLING method to other 3D methods such as 3D radial and

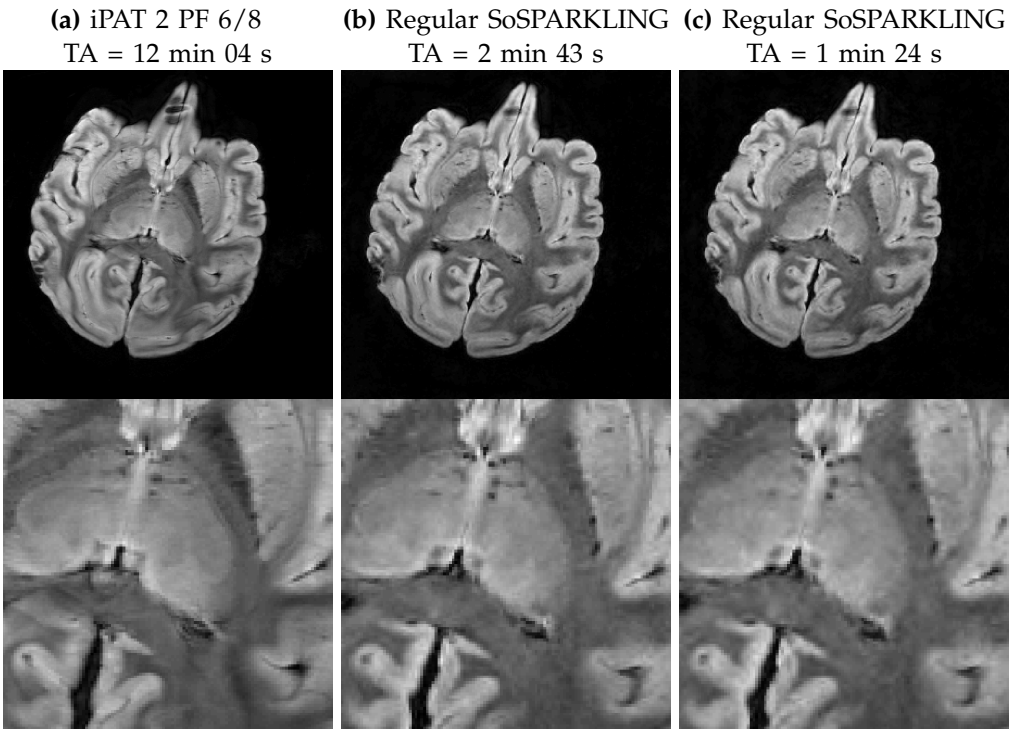

Fig. 7. *Ex vivo* results of high in plane resolution of 0.3 mm and 1.5-mm slice thickness for 96 slices. **(a)**, the reference Cartesian scan used iPAT 2 with partial Fourier 6/8 (phase and slice encode) and lasted 12 min 04 s. The two Regular stack-of-sparkling (SoSPARKLING) schemes were composed of 2090 shots **(b)** and 4085 shots **(c)**, corresponding to acquisition times of 1 min 24 s and 2 min 43 s, respectively. FOV was $200 \times 200 \times 140$ mm^3.

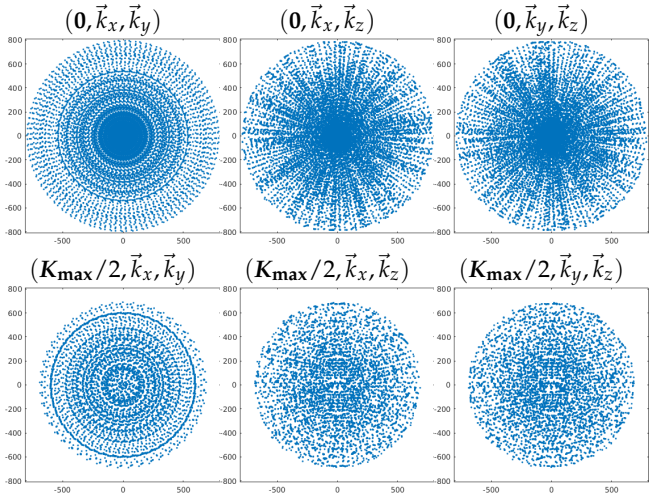

Fig. 8. From left to right: plane sections of an isotropic fully 3D SPARKLING trajectory showing all the samples contained in a plane of thickness one k-space pixel ($1/FOV$). The plane sections are crossing the origin $\mathbf{0} = (0,0,0)$ (top row) of the k-space or half the maximum spatial frequency $\boldsymbol{K}_{\mathbf{max}}/2 = (\frac{K_{\max}}{2}, \frac{K_{\max}}{2}, \frac{K_{\max}}{2})$ (bottom row) for different directions. Because of isotropy, we used the same $K_{\max}$ over all axes.

the Poisson-disk lines proposed by Lustig et al., for the same acquisition time of 45 s. The proposed method performed significantly better than these two techniques which both appear blurry, showing the limitations of sampling along lines only. Interestingly, this shows that in 3D, the Poisson-disk lines method is not adapted to all imaging scenarios using compressed sensing: it may be interesting for short readouts but for longer readouts applications such as T2* weighted imaging (e.g. SWI) it is not as efficient as the SPARKLING approach. In this regard, the recent wave-CAIPI strategy [36] also improves the sampling efficiency by using an analytical corkscrew waveform instead of a straight line. However, this pseudo-Cartesian method which seeks to spread the aliasing in all three dimensions to allow full utilization of coil sensitivity profiles was not proposed in the context compressed sensing and its extension to variable density sampling is not clear.

For a high in plane resolution of 0.3 mm, a slice thickness of 1.5 mm and a FOV of $200 \times 200 \times 140$ mm^3, the SPARKLING method was also able to significantly reduce the acquisition time. Compared to the standard sequence used in the context of high resolution SWI (iPAT 2 Partial Fourier 6/8) which lasted 12 min 04 s, the proposed method yielded a similar image quality in only 1 min 24 s. Perhaps, the acceleration could be pushed even further and enable to reduce the acquisition time below one minute while still presenting diagnostic image quality.

As long as the readout duration and the gradient constraints allow the SPARKLING trajectories to deviate from the initial input pattern, our method should lead to better image quality than predetermined parameterized families such as spirals or lines since all the versatility of the gradients is exploited. However, let us emphasize that the longer the readouts, the more we should expect from SPARKLING, since more circumvolutions are al-

lowed. T_2^* weighted imaging therefore better illustrates the advantages of the method.

These encouraging *ex vivo* results are yet to be fully validated with *in vivo* acquisitions for which off-resonance effects may be a concern. We however expect the 3D SPARKLING trajectories to show the same relative robustness to B0 inhomogeneities as their 2D counterparts [16]. Regarding gradient imperfections, the quality of our *ex vivo* results suggest that the 3D SPARKLING trajectories are performed accurately by our gradient system, although this aspect should be studied further [37], [38].

VII. Conclusions

In this work, we proposed to use a variable-density SPARKLING strategy to accelerate the scan time of high resolution T_2^*-weighted 3D acquisitions. Among the three studied approaches of 3D SPARKLING, it was observed that a stack-of-SPARKLING with variable density and number of shots along the partition direction was performing best. Compared to a reference iPAT4 Cartesian scan, the proposed method allowed to divide the acquisition time by a factor of 20, while maintaining good image quality at a 0.6 mm isotropic resolution. Moreover, we compared SPARKLING to other 3D variable-density sampling such as 3D radial and the Poisson-disk-lines, for an isotropic resolution of 0.6 mm and a constant acquisition time of 45 s. In the presented *ex vivo* experiments, the proposed method performed significantly better than these two techniques which both appeared blurry. Finally, the 3D SPARKLING method was also used for a very high in plane resolution of 0.3 mm and was shown to maintain a good image quality in just 2 minutes compared to the reference Cartesian scan of 12 minutes. A straightforward application may be ultrafast 3D susceptibility-weighted imaging [23].

Acknowledgements

This research program was supported by a 2016 DRF Impulsion grant (COSMIC, P.I.: P.C.). C.L. was also supported by the CEA international PhD program. P.W. was supported by the ANR JCJC OMS. We would like to thank Nicolas Boulant for his insightful remarks. The authors are thankful to Dr Patrick Martigne (Department of Radiobiology, IRBA, Brétigny-sur-Orge, France) for the preparation of the *ex vivo* baboon brain.

References

[1] M. Lustig, D. Donoho, and J. M. Pauly, "Sparse MRI: The application of compressed sensing for rapid MR imaging," *Magnetic Resonance in Medicine*, vol. 58, no. 6, pp. 1182–1195, 2007.

[2] G. Puy, P. Vandergheynst, and Y. Wiaux, "On variable density compressive sampling," *IEEE Signal Processing Letters*, vol. 18, no. 10, pp. 595–598, 2011.

[3] B. Adcock, A. C. Hansen, C. Poon, and B. Roman, "Breaking the coherence barrier: A new theory for compressed sensing," vol. 5, 2017.

[4] C. Boyer, J. Bigot, and P. Weiss, "Compressed sensing with structured sparsity and structured acquisition," *Applied and Computational Harmonic Analysis*, 2017.

[5] P. E. Larson, P. T. Gurney, and D. G. Nishimura, "Anisotropic field-of-views in radial imaging," *IEEE Transactions on Medical Imaging*, vol. 27, no. 1, pp. 47–57, 2008.

[6] S. S. Vasanawala, M. T. Alley, B. A. Hargreaves, R. A. Barth, J. M. Pauly, and M. Lustig, "Improved pediatric MR imaging with compressed sensing," *Radiology*, vol. 256, no. 2, pp. 607–616, 2010.

[7] P. Irarrazabal and D. G. Nishimura, "Fast three dimensional magnetic resonance imaging," *Magnetic Resonance in Medicine*, vol. 33, no. 5, pp. 656–662, 1995.

[8] F. E. Boada, J. S. Gillen, G. X. Shen, S. Y. Chang, and K. R. Thulborn, "Fast three dimensional sodium imaging," *Magnetic Resonance in Medicine*, vol. 37, no. 5, pp. 706–715, 1997.

[9] G. Valvano, N. Martini, L. Landini, and M. F. Santarelli, "Variable density randomized stack of spirals(VDR-SoS) for compressive sensing MRI," *Magnetic Resonance in Medicine*, vol. 76, no. 1, pp. 59–69, 2016.

[10] K. M. Johnson, "Hybrid radial-cones trajectory for accelerated MRI," *Magnetic Resonance in Medicine*, vol. 77, no. 3, pp. 1068–1081, 2017.

[11] B. M. Dale, J. S. Lewin, and J. L. Duerk, "Optimal design of *k*-space trajectories using a multi-objective genetic algorithm," *Magnetic Resonance in Medicine*, vol. 52, no. 4, pp. 831–841, 2004.

[12] R. Mir, A. Guesalaga, J. Spiniak, M. Guarini, and P. Irarrazaval, "Fast three-dimensional *k*-space trajectory design using missile guidance ideas," *Magnetic Resonance in Medicine*, vol. 52, no. 2, pp. 329–336, 2004.

[13] C. Kumar Anand, A. Thomas Curtis, and R. Kumar, "Durga: A heuristically-optimized data collection strategy for volumetric magnetic resonance imaging," *Engineering Optimization*, vol. 40, no. 2, pp. 117–136, 2008.

[14] N. Chauffert, P. Ciuciu, J. Kahn, and P. Weiss, "A projection method on measures sets," *Constructive Approximation*, vol. 45, no. 1, pp. 83–111, 2017.

[15] C. Boyer, N. Chauffert, P. Ciuciu, J. Kahn, and P. Weiss, "On the generation of sampling schemes for magnetic resonance imaging," *SIAM Journal on Imaging Sciences*, vol. 9, no. 4, pp. 2039–2072, 2016.

[16] C. Lazarus, P. Weiss, N. Chauffert, F. Mauconduit, L. El Gueddari, C. Destrieux, I. Zemmoura, A. Vignaud, and P. Ciuciu, "SPARKLING: variable-density k-space filling curves for accelerated T2*-weighted MRI," *Magnetic Resonance in Medicine*, Jan. 2019.

[17] H. K. Song and L. Dougherty, "Dynamic MRI with projection reconstruction and KWIC processing for simultaneous high spatial and temporal resolution," *Magnetic Resonance in Medicine*, vol. 52, no. 4, pp. 815–824, 2004.

[18] W. Lin, J. Guo, M. A. Rosen, and H. K. Song, "Respiratory motion-compensated radial dynamic contrast-enhanced (DCE)-MRI of chest and abdominal lesions," *Magnetic Resonance in Medicine*, vol. 60, no. 5, pp. 1135–1146, 2008.

[19] D. R. Thedens, P. Irarrazaval, T. S. Sachs, C. H. Meyer, and D. G. Nishimura, "Fast magnetic resonance coronary angiography with a three-dimensional stack of spirals trajectory," *Magnetic Resonance in Medicine*, vol. 41, no. 6, pp. 1170–1179, 1999.

[20] P. Börnert and D. Jensen, "Coronary artery imaging at 0.5 T using segmented 3D echo planar imaging," *Magnetic Resonance in Medicine*, vol. 34, no. 6, pp. 779–785, 1995.

[21] L. Kasper, M. Engel, C. Barmet, J. Reber, J. Heinzle, K. E. Stephan, and P. K. Paul, "Rapid 3D blipped spiral fMRI at 7 T," in *Proc. Intl. Soc. Mag. Reson. Med.*, vol. 26, no. 5461, 2018.

[22] D. Stäb, S. Bollmann, C. Langkammer, K. Bredies, and M. Barth, "Accelerated mapping of magnetic susceptibility using 3D planes-on-a-paddlewheel (POP) EPI at ultra-high field strength," *NMR in Biomedicine*, vol. 30, no. 4, p. e3620, 2017.

[23] A. Abosch, E. Yacoub, K. Ugurbil, and N. Harel, "An assessment of current brain targets for deep brain stimulation surgery with susceptibility-weighted imaging at 7 Tesla," *Neurosurgery*, vol. 67, no. 6, pp. 1745–1756, 2010.

[24] C. Lenglet, A. Abosch, E. Yacoub, F. De Martino, G. Sapiro, and N. Harel, "Comprehensive in vivo mapping of the human basal ganglia and thalamic connectome in individuals using 7T MRI," *PloS One*, vol. 7, no. 1, p. e29153, 2012.

[25] C. Moenninghoff, O. Kraff, S. Maderwald, L. Umutlu, J. M. Theysohn, A. Ringelstein, K. H. Wrede, C. Deuschl, J. Altmeppen, M. E. Ladd *et al.*, "Diffuse axonal injury at ultra-high field MRI," *PLoS One*, vol. 10, no. 3, p. e0122329, 2015.

[26] N. Chauffert, P. Weiss, J. Kahn, and P. Ciuciu, "A projection algorithm for gradient waveforms design in Magnetic Resonance Imaging," *IEEE Transactions on Medical Imaging*, vol. 35, no. 9, pp. 2026–2039, Sep. 2016.

[27] C. Schmaltz, P. Gwosdek, A. Bruhn, and J. Weickert, "Electrostatic halftoning," in *Computer Graphics Forum*, vol. 29, no. 8. Wiley Online Library, 2010, pp. 2313–2327.

[28] T. Teuber, G. Steidl, P. Gwosdek, C. Schmaltz, and J. Weickert, "Dithering by differences of convex functions," *SIAM Journal on Imaging Sciences*, vol. 4, no. 1, pp. 79–108, 2011.

[29] P. Leopardi, "A partition of the unit sphere into regions of equal area and small diameter," *Electronic Transactions on Numerical Analysis*, vol. 25, no. 12, pp. 309–327, 2006.

[30] S. Lloyd, "Least squares quantization in PCM," *IEEE Transactions on Information Theory*, vol. 28, no. 2, pp. 129–137, 1982.

[31] M. A. Schmidt, T. Engelhorn, F. Marxreiter, J. Winkler, S. Lang, S. Kloska, P. Goelitz, and A. Doerfler, "Ultra high-field SWI of the substantia nigra at 7T: reliability and consistency of the swallow-tail sign," *BMC neurology*, vol. 17, no. 1, p. 194, 2017.

[32] L. El Gueddari, C. Lazarus, H. Carrié, A. Vignaud, and P. Ciuciu, "Self-calibrating nonlinear reconstruction algorithms for variable density sampling and parallel reception MRI," in *10th IEEE Sensory Array and Multichannel (SAM) signal processing workshop*, Sheffield, UK, Jul. 2018, pp. 415–419.

[33] J. Keiner, S. Kunis, and D. Potts, "Using NFFT 3—A Software Library for Various Nonequispaced Fast Fourier Transforms," *ACM Transactions on Mathematical Software (TOMS)*, vol. 36, no. 4, p. 19, 2009.

[34] J.-M. Lin, "Python Non-Uniform Fast Fourier Transform (PyNUFFT): An Accelerated Non-Cartesian MRI Package on a Heterogeneous Platform (CPU/GPU)," *Journal of Imaging*, vol. 4, no. 3, p. 51, 2018.

[35] Z. Wang, A. C. Bovik, H. R. Sheikh, and E. P. Simoncelli, "Image quality assessment: from error visibility to structural similarity," *IEEE Transactions on Image Processing*, vol. 13, no. 4, pp. 600–612, 2004.

[36] B. Bilgic, B. A. Gagoski, S. F. Cauley, A. P. Fan, J. R. Polimeni, P. E. Grant, L. L. Wald, and K. Setsompop, "Wave-CAIPI for highly accelerated 3D imaging," *Magnetic Resonance in Medicine*, vol. 73, no. 6, pp. 2152–2162, 2015.

[37] B. E. Dietrich, D. O. Brunner, B. J. Wilm, C. Barmet, S. Gross, L. Kasper, M. Haeberlin, T. Schmid, S. J. Vannesjo, and K. P. Pruessmann, "A field camera for MR sequence monitoring and system analysis," *Magnetic Resonance in Medicine*, vol. 75, no. 4, pp. 1831–1840, 2016.

[38] S. J. Vannesjo, N. N. Graedel, L. Kasper, S. Gross, J. Busch, M. Haeberlin, C. Barmet, and K. P. Pruessmann, "Image reconstruction using a gradient impulse response model for trajectory prediction," *Magnetic Resonance in Medicine*, vol. 76, no. 1, pp. 45–58, 2016.